Journal of Zhejiang University-SCIENCE A (Applied Physics & Engineering) 2023 24(12):1065-1078
www.jzus.zju.edu.cn; www.springer.com/journal/11582
E-mail: jzus_a@zju.edu.cn

Research Article

https://doi.org/10.1631/jzus.A2300589

Enhanced mixing efficiency for a novel 3D Tesla micromixer for Newtonian and non-Newtonian fluids

Abdellah AAZMI[1,2], Zixian GUO[1,2], Haoran YU[1,2], Weikang LV[1,2], Zengchen JI[1,2], Huayong YANG[1,2], Liang MA[1,2]✉

[1]*State Key Laboratory of Fluid Power and Mechatronic Systems, Zhejiang University, Hangzhou 310058, China*
[2]*School of Mechanical Engineering, Zhejiang University, Hangzhou 310058, China*

Abstract: The fabrication of constructs with gradients for chemical, mechanical, or electrical composition is becoming critical to achieving more complex structures, particularly in 3D printing and biofabrication. This need is underscored by the complexity of in vivo tissues, which exhibit heterogeneous structures comprised of diverse cells and matrices. Drawing inspiration from the classical Tesla valve, our study introduces a new concept of micromixers to address this complexity. The innovative micromixer design is tailored to enhance the re-creation of in vivo tissue structures and demonstrates an advanced capability to efficiently mix both Newtonian and non-Newtonian fluids. Notably, our 3D Tesla valve micromixer achieves higher mixing efficiency with fewer cycles, which represents a significant improvement over the traditional mixing method. This advance is pivotal for the field of 3D printing and bioprinting, and offers a robust tool that could facilitate the development of gradient hydrogel-based constructs that could also accurately mimic the intricate heterogeneity of natural tissues.

Key words: Micromixing; 3D printing; Non-Newtonian fluids; Computational fluid dynamics

1 Introduction

The construction of gradient multimaterials has become critical in various fields, notably in 3D printing and bioprinting (Liu et al., 2017; Kokkinis et al., 2018; Skylar-Scott et al., 2019; Ramezani et al., 2020; Zhou et al., 2022). Multimaterial 3D printing plays a pivotal role in replicating in vivo tissues by fostering an optimal microenvironment for tissue growth and development (Tavafoghi et al., 2021; Aazmi et al., 2022, 2024). Gradient structure hydrogels, which are fabricated using 3D printing, are instrumental in accurately mimicking the complex spatial arrangement of components in the cellular and extracellular matrices, which is a prerequisite for the successful fabrication of biological tissue (Monzón, 2018; Chen et al., 2021; Zhang et al., 2022).

✉ Liang MA, liangma@zju.edu.cn
Liang MA, https://orcid.org/0000-0002-6242-1850

Received Nov. 20, 2023; Revision accepted Dec. 6, 2023;
Crosschecked Dec. 18, 2023

Extrusion-based 3D printing is a prominent additive manufacturing method known for its scalability and compatibility with other biofabrication techniques (Zhang et al., 2019). It is a promising approach that is used to 3D print bioactive structures that have continuous gradients (Mehta and Rath, 2021; Tavafoghi et al., 2021). However, the development of efficient micromixers for gradient 3D printing remains a significant challenge that has been marked by trials and innovations. Traditional micromixer designs, despite the diversity of their channel geometries and flow dynamics, often face limited mixing efficiency, particularly with high-viscosity fluids. This inefficiency can lead to inhomogeneity in the printed structure and the risk of channel blockages, which pose a significant barrier to creating the uniform gradient tissues that are essential to maintaining cell viability and the desired tissue architecture.

The limitations of current micromixer technologies highlight the need for a new paradigm. A design that accommodates a broader range of hydrogels, encompasses various fluid viscosities, and ensures consistent, high-fidelity mixing is needed. Recent advancements, such as the integration of the

Kenics static mixer (KSM) in extrusion bioprinting, represent significant progress (Chávez-Madero et al., 2020; Bolívar-Monsalve et al., 2021; Holmberg et al., 2021). Despite the invention of the KSM over fifty years ago (Armeniades et al., 1966), the incorporation of modern 3D printing techniques, especially stereolithography (SLA), has facilitated the creation of intricate and complex structures and opened new avenues of innovation in micromixer design (Xiong et al., 2022). Another widely used micromixer is the Tesla micromixer, which represents a class of passive devices that harness the design principles of Tesla valves to facilitate efficient fluid mixing at the microscale (Abolpour et al., 2022; Buglie et al., 2022). Tesla valves, which are named after their inventor Nikola Tesla, are inherently unidirectional; they allow fluid to flow preferentially in one direction and impede it in the opposite direction. This characteristic is leveraged within the micromixer to induce recirculation zones, which are instrumental in augmenting fluid mixing with the use of both diffusive and advective phenomena (Abolpour et al., 2022). However, this micromixer has not yet been used in 3D printing applications.

In this study, we introduce a novel micromixer design that is based on the Tesla valve and that demonstrates a heightened ability to achieve superior mixing efficiency with fewer mixing cycles. Utilizing computational fluid dynamics (CFD) simulations, we meticulously analyze both Newtonian and non-Newtonian fluids to assess mixing efficiency and other critical dimensionless parameters. This approach provides us with a deeper understanding of the intricate processes that occur within the micromixer. Crucially, experimental validations confirm that our micromixer can efficiently blend hydrogels and demonstrates a high degree of reproducibility. This advancement holds significant promise for enhancing the precision and consistency of bioprinted structures and represents a substantial leap forward in the realm of tissue engineering and regenerative medicine.

2 Materials and methods

2.1 Preparation of GelMA, porous GelMA, and alginate hydrogels

The GelMA (EFL-GM30) and porous GelMA (PGM) (EFL-GM-PR 001) used for this study were obtained from EFL Inc. (Suzhou, China). The porous GelMA (EFL-GM-PR-001) consists of GelMA (M_w= 150 kDa, degree of substitution: 60%), polyethylene oxide (M_w=300 kDa), and photoinitiator lithium phenyl-2,4,6-trimethylbenzoylphosphinate (LAP) in a mass ratio of 100/15/5. For the initial preparation of porous GelMA hydrogel, 0.0025 g/mL of the LAP was dissolved in phosphate-buffered saline (PBS) to create a homogenous LAP solution. Subsequently, the bulk porous GelMA was mixed with the LAP solution, and the mixture was continuously stirred for 1 h at 37 °C in a water bath, thereby producing a 0.06 g/mL porous GelMA hydrogel and similarly producing a 0.06 g/mL GM30.

Alginate-based hydrogels were selected for this study due to their prominence in bioprinting research, which is attributable to their favorable biocompatibility and tunable mechanical properties (Rastogi and Kandasubramanian, 2019; Agrawal et al., 2023). Alginate at a concentration of 0.035 g/mL in a 0.035 g/mL $CaCl_2$ crosslinking solution was used to explore the mixing efficiency of the newly designed micromixer for handling non-Newtonian fluids. The chosen concentration aligns with the commonly utilized ranges in bioprinting and provides a relevant context for an evaluation of the micromixer's performance.

To prepare the hydrogel, the alginate and $CaCl_2$ were both sourced from Cellink (Gothenburg, Sweden) to prepare the desired 0.035 g/mL concentration of alginate hydrogel. This solution was then sterile-filtered into a 15 mL Falcon tube via a syringe fitted with a sterile 0.22 μm syringe filter to ensure the sterility and homogeneity of the hydrogel.

To ensure a clear view of the diffusion phenomena in the hydrogels, two color dyes from NJDULY (Nanjing, China) were used: blue (Erioglaucine disodium salt) and yellow (tartrazine).

2.2 Printing setup

We utilized a custom-designed 3D printing apparatus equipped with independently controlled *X*, *Y*, and *Z* axes with three precision pumps. For this study, two of these pumps were dedicated to extruding biocompatible inks of different colors. The system's motion platform was controlled using pulse-width modulation signals generated by a computer, which were then relayed to servo motors. This configuration allowed for meticulous manipulation of both the

platform's spatial positioning and the extrusion velocity, which ensured the high-precision deposition of the inks. The extrusion speed that we used was equivalent to 0.08 mm/s in a 2 mm diameter channel. Droplets were printed to assess the mixing performance of our micromixer. The pictures of the printed drops were taken using a charge-coupled device (CCD) camera.

2.3 Rheological characterization

The rheological behaviors of various hydrogels (0.06 g/mL PGM and 0.06 g/mL GM30) were assessed using an MCR302 rheometer (Anton Paar, Austria), which featured Peltier elements for precise temperature control. In the temperature sweep test, each hydrogel sample was initially equilibrated to 40 °C. It was then placed onto the rheometer's preheated substrate, which was also maintained at 40 °C. We ensured that the 1 mm gap between the substrate and the 50 mm diameter tapered plate rotor was filled. The hydrogel's viscoelastic properties were measured by gradually cooling it from 37 to 4 °C at a controlled rate of 2 °C/min while holding the shear rate constant at 1 s^{-1}.

2.4 Micromixer design and fabrication

The proposed 3D Tesla micromixer was designed with two main sections (Fig. 1a). The first section aids in creating a coaxial flow, which sets the stage for effective mixing. The subsequent section, which forms the core of our micromixer, consists of symmetric Tesla elements (Fig. 1a). These elements are pivotal to the mixer's functionality, and we prioritized the development of these Tesla elements in our design process. This involved conducting a series of simulations, the results of which were then rigorously compared with the experimental data. This comparative analysis was crucial to validating our CFD models and ensuring the reliability and effectiveness of the mixer's design.

During the development of our 3D Tesla micromixer, the design process commenced with the CFD simulation of the 2D Tesla valve elements. Through these simulations, optimal dimensions and geometrical configurations were determined, and they served as a foundation for the subsequent transition to a 3D architecture. Transitioning from a 2D to a 3D design entails a complex re-evaluation of fluid dynamics due to the additional spatial complexity, which necessitates rigorous validation and verification. These steps are critical to confirming that the enhancements predicted by the CFD models hold in practical scenarios. This will be elaborated upon in subsequent sections of this manuscript.

As illustrated in Fig. 1b, the innovative 3D design strategically optimizes the spatial arrangement and specific geometries of the Tesla valves to maximize their mixing efficiency. This optimized design induces controlled turbulence and complex, chaotic flow patterns, which significantly improve the mixing capabilities. Moreover, particular attention is dedicated to refining features that reduce the pressure drop across the micromixer and achieve a more uniform flow distribution, thereby enhancing the mixing efficacy without degrading the fluid throughput.

Finally, the micromixer was fabricated using precise SLA 3D printing technology. Transparent resin was used during printing so that the mixing process in the micromixer could be observed. Four micromixer types were constructed, including one-cycle, two-cycle, three-cycle, and four-cycle micromixers.

2.5 Numerical methods

2.5.1 Governing equations

A simulation of the micromixing process within a 3D Tesla micromixer is governed by the concentration distribution equation:

$$u \cdot \nabla c = D\nabla^2 c, \tag{1}$$

where u is the flow velocity, c is the species concentration, and D denotes the diffusion coefficient. The boundary conditions are considered to be:

$$\begin{cases} u = u_0, & \text{on } \Gamma_{\text{inlet}}, \\ u = 0, & \text{on } \Gamma_{\text{wall}}, \\ u = 0, & \text{on } \Gamma_{\text{outlet}}, \\ c = c_0, & \text{on } \Gamma_{\text{inlet}}, \end{cases} \tag{2}$$

where Γ_{inlet}, Γ_{outlet}, and Γ_{wall} are the inlet, outlet, and wall of the fluid domain, respectively. u_0 and c_0 are the initial flow velocity and concentration, respectively.

In our study, we will deal with both Newtonian (GelMA and porous GelMA hydrogel at 25 °C) and power-law non-Newtonian fluids (alginate hydrogel)

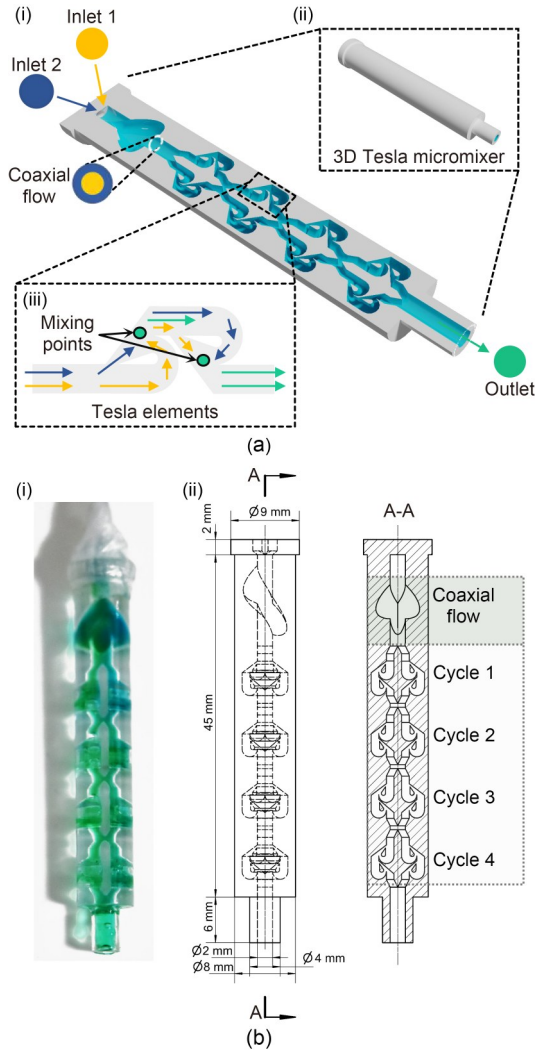

Fig. 1 Overview of the 3D Tesla micromixer design and operational flow dynamics: (a) a cutaway illustration (i) of the 3D Tesla micromixer (ii) and the internal Tesla elements (iii), with inlets 1 and 2 initiating coaxial flow that leads to subsequent mixing points; (b) a real-world implementation of the micromixer (i) alongside a diagrammatic representation of the flow pattern across four mixing cycles (ii), illustrating the repeated folding and splitting action that is characteristic of Tesla mixing elements, culminating in an efficient coaxial mixing process

(Florián-Algarín and Acevedo, 2010; Ma et al., 2014; Rodríguez-Rivero et al., 2014; Poologasundarampillai et al., 2021). For the Newtonian fluids, the viscosity is considered to be constant at 25 °C. For the non-Newtonian fluid dynamics within the 3D Tesla micromixer, a power-law model was employed to describe the rheology of alginate hydrogel. This model is particularly well-suited to fluids whose viscosity changes with the rate of shear, characterized by the flow behavior index n and the consistency index K. In the power-law model, the apparent viscosity μ is described by the relationship:

$$\mu = K\dot{\gamma}^{n-1}, \tag{3}$$

where $\dot{\gamma}$ is the shear rate. For shear-thinning fluids, $n<1$, and for shear-thickening fluids, $n>1$ (Becker, 1980; Khandelwal et al., 2015). The consistency index K is a measure of the fluid's resistance to flow; higher values of K indicate a more viscous fluid (Becker, 1980).

2.5.2 Reynolds and Péclet numbers

The Reynolds number (Re) is an important dimensionless parameter in fluid mechanics that is introduced to characterize the flow in the system. The Re is the ratio of the inertial effects to viscous effects, defined as follows for Newtonian flows:

$$Re_{\mathrm{N}} = \frac{\rho U L}{\mu_{\infty}}, \tag{4}$$

and as follows for non-Newtonian power-law models (King, 2002):

$$Re_{\mathrm{PL}} = \frac{\rho U_{\mathrm{PL}}^{2-n} L^{n}}{\frac{K}{8}\left(\frac{6n+2}{n}\right)^{n}}, \tag{5}$$

where ρ denotes the fluid density, U is the characteristic velocity of Newtonian fluid, U_{PL} is the characteristic velocity of non-Newtonian power-law flow fluid (defined as the average velocity at the inlet boundary, which will be defined later in Eq. (7)), L represents the characteristic length scale (width of the inlet in this study), and μ_{∞} is the fluid's infinite shear-rate viscosity.

During our examination of the mixing efficiency and species transport within the 3D Tesla micromixer, the Péclet number (Pe) emerged as a pivotal dimensionless parameter. The Péclet number is defined as the ratio of the advective transport rate to the diffusive transport rate and is given by

$$Pe = \frac{UL}{D}, \tag{6}$$

where D is the diffusion coefficient of the species being mixed.

For non-Newtonian fluids in laminar flow, the flow velocity can be written as follows (King, 2002):

$$U_{\mathrm{PL}}=\frac{nL}{2(3n+1)}\left(\frac{\tau_{\mathrm{w}}}{K}\right)^{\frac{1}{n}}, \tag{7}$$

where τ_{w} represents the shear stress in the wall of the pipe. Therefore, by replacing in Eq. (6), we calculate the Péclet number for the power-law (Pe_{PL}) as follows:

$$Pe_{\mathrm{PL}}=\frac{nL^2}{2(3n+1)D}\left(\frac{\tau_{\mathrm{w}}}{K}\right)^{\frac{1}{n}}. \tag{8}$$

In the micromixing process, a high Péclet number indicates that advection strongly dominates over diffusion (Nguyen and Wu, 2005). In contrast, a low Péclet number suggests that diffusion is the predominant mechanism for species transport. The design of the 3D Tesla micromixer is intended to optimize the interplay between these two transport phenomena to achieve a homogeneous mixture within the shortest possible distance along the flow path.

2.5.3 Mixing efficiency

To ensure the authenticity of the experimental results and convincingly assess the mixing efficiency of our 3D Tesla micromixer, it is critical to introduce a quantitative calculation of mixing performance in addition to the contour plot generated by the simulation software. As has been previously reported, the mixing efficiency of a static mixer can be analyzed using a statistical measurement method based on the concept of the intensity of segregation (Nguyen and Wu, 2005; Bayareh et al., 2020). The quantification of mixing efficiency can be achieved with the following equation, using the mixing index MI at a cross-section perpendicular to the flow direction:

$$\mathrm{MI}=\sqrt{\frac{\sigma^2}{\sigma_{\max}^2}}, \tag{9}$$

where σ^2 refers to the actual variance, and $\sigma_{\max}^2$ is the maximum possible variance on a cross-sectional plane vertical to the flow direction. σ^2 is defined as

$$\sigma^2=\frac{1}{N}\sum_{i=1}^{N}(c_i-\bar{c})^2, \tag{10}$$

where c_i is the mass fraction at the ith sampling point, $\bar{c}$ is the optimal mixing mass fraction, and N is the number of sampling points on the corresponding plane. The maximum variance ($\sigma_{\max}^2$) can be calculated as follows:

$$\sigma_{\max}^2=\bar{c}(1-\bar{c}). \tag{11}$$

The optimal mass fraction ($\bar{c}$) at the cut-plane is equal to 0.5 under symmetrical boundary conditions. Considering this, $\sigma_{\max}^2$ is considered to be equal to 0.25 when there is equal flow in the fluid streams. The value of MI ranges from 0 (unmixed initial state) to 1 (thoroughly mixed). Thus, as the value of MI increases, we know that the mixing performance is improving. On the contrary, a low MI value indicates that the mixing is insufficient. However, it has been reported that the numerical results may overestimate the mixing efficiency due to numerical diffusion.

2.6 CFD model and boundary conditions

Numerical simulation was carried out using the CFD module in the COMSOL Multiphysics finite element package (Version 5.6, COMSOL Co., Ltd., Sweden) to simulate the velocity profiles within the 3D micromixer. The operating conditions were that the fluids were treated as incompressible, and no-slip boundary conditions for all walls were applied and the outlet pressure was zero in the computational analysis. The inlet velocities were considered to be fully developed, with velocities equivalent to the extrusion rate of the hydrogels in the bioprinting applications (0.01, 0.02, 0.04, 0.08, and 0.16 mm/s in a cylinder having a diameter of 2 mm). Numerical models of the 3D micromixers with different geometry parameters were built (Fig. 2). The number of Tesla elements and their flow fields were solved to analyze the mixing mechanism. Regarding the properties of the materials used, the diffusion coefficient for PBS was assigned a value of 6×10^{-10} m^2/s. In comparison, the GM30 had a diffusion coefficient of 3×10^{-10} m^2/s, whereas both the PGM and the alginate hydrogel were assigned a diffusion coefficient of 1×10^{-10} m^2/s. The power-law model parameters for the 0.035 g/mL alginate hydrogel were adopted from a study by Sánchez-Sánchez

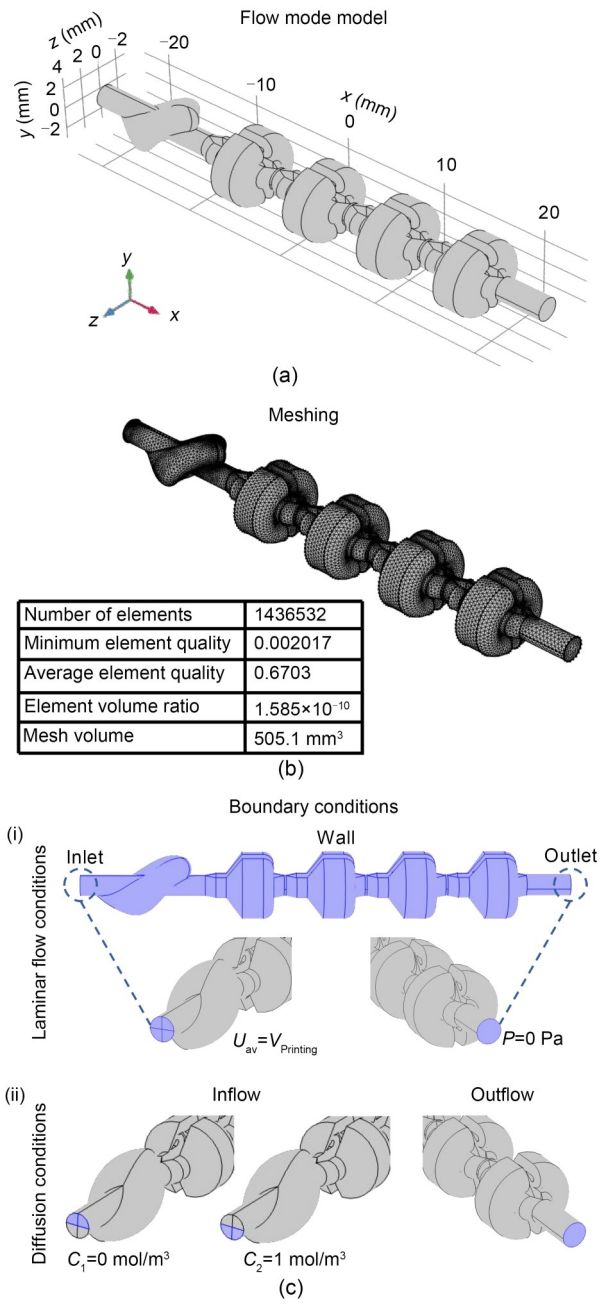

Fig. 2 Schematic representation of the micromixer design and computational fluid dynamics (CFD) simulation model: (a) flow mode model illustrating the complete micromixer geometry, including the arrangement of the Tesla structures that were designed to enhance mixing; (b) meshing detail showing the discretized elements used for the CFD simulation; (c-i) laminar flow boundary conditions specified for the inlets and outlets to define the fluid velocity profile in the inlet as a developed flow with an average velocity U_{av}, which is equal to the printing speed $V_{Printing}$, and pressure condition at the outlet P; (c-ii) diffusion conditions set at the inlets with contrasting concentration boundaries (C_1=0 mol/m^3 for inlet 1, and C_2=1 mol/m^3 for inlet 2) to simulate the mixing of two distinct fluids within the device

et al. (2023). The viscosity values for PGM and GM30 were determined from the rheological characterization previously mentioned.

3 Results and discussion

3.1 Model validation

To corroborate the CFD model, experimental measurements of the pressure drop across the 3D Tesla micromixer were taken. These measurements are considered to be the most adequate criterion for evaluating the correctness of the CFD micromixer simulation (Nyande et al., 2021; Valdés et al., 2022). The experimental setup consisted of a syringe pump to control the flow rate through the micromixer. Pressure transducers were installed at both the inlet and outlet to measure the differential pressure. The steady-state pressure for each flow rate was recorded, and the system reached equilibrium before the measurements were taken. The pressure drop, ΔP, across the micromixer was determined by

$$\Delta P = P_{\text{inlet}} - P_{\text{outlet}}, \tag{12}$$

where P_{inlet} and P_{outlet} represent the measured pressures at the inlet and outlet, respectively. To ensure the fidelity of the experimental conditions during the simulation, the fluids were maintained at a constant temperature of 25 °C, as GM30 and PGM were shown to have the same viscosity at this temperature (Fig. 3a), which means that they could be considered Newtonian fluids, and their properties were matched to the simulation parameters.

These experimental findings were subsequently plotted and compared with the simulation data to evaluate the predictive accuracy of the model (Fig. 3b).

This experimental validation process is a crucial step to ensuring that the 3D Tesla micromixer operates as predicted by the simulations when it is applied in practical scenarios, such as in bioprinting applications where precise fluid control is needed.

3.2 Effect of the number of 3D Tesla micromixer cycles on mixing performance

In this computational study, the effects of Tesla structure multiplicity on the mixing efficiency of a

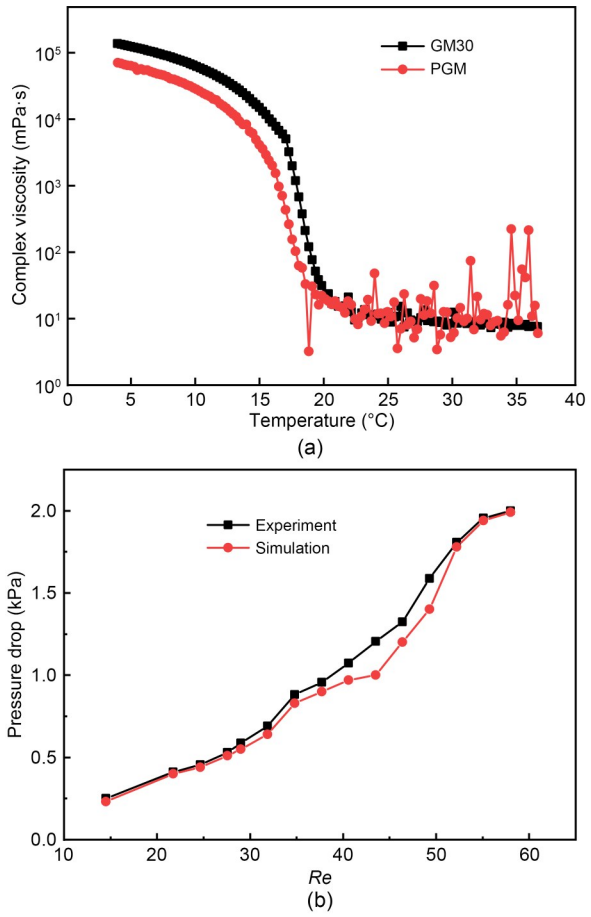

Fig. 3 Comparative analysis of the rheological properties and pressure drop of the micromixer: (a) rheological behaviors of GM30 and PGM, where the viscosity is depicted as a function of shear rate; (b) correlation of experimental data with simulation results for the pressure drop across the micromixer

micromixer device were explored. Simulations were constructed to understand how the incorporation of multiple cycles—where each cycle is a single Tesla element—affects the homogeneity of fluid mixing at the microscale (Fig. 4). The results elucidate the interplay between fluid dynamics and mixer geometry in the context of the laminar flow regimes that are typically encountered in microfluidic applications.

Our analysis reveals a clear trend of increased mixing efficiency with additional cycles; however, this improvement is not linear. With the initial introduction of a second Tesla cycle, we observed a substantial increase in the mixing efficiency, from 75.95% to 83.58%. This significant increase underscores the impact of the fluid folding and chaotic advection mechanisms that were initiated by the Tesla structures.

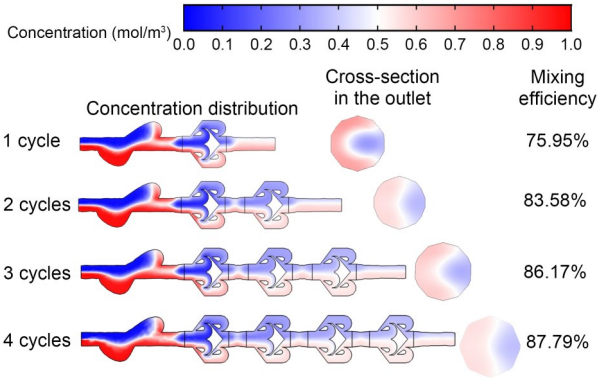

Fig. 4 Simulation results that depict progressive mixing efficiency across multiple cycles (1, 2, 3, and 4 cycles) of the 3D Tesla micromixer

However, the subsequent additions of the third and fourth cycles yielded a lesser increase in efficiency to 86.17% and 87.79%, respectively. This pattern indicates an approach toward an asymptotic limit and suggests that a saturation point may exist where the benefits of additional Tesla structures are outweighed by practical considerations such as an increased pressure drop, longer residence times, and design complexity.

The diminishing returns observed with an increase in the cycle numbers raise critical questions about the scalability of this approach. The balance between the efficiency gains and the additional complexity (and potential cost) of integrating additional Tesla structures must be carefully weighed for practical applications. This is especially pertinent in high-throughput systems where the marginal gains of mixing efficiency may not justify the corresponding increase in the pressure requirements or the device footprint. Furthermore, although this study assumes that the fluids behave as Newtonian fluids for simplicity, fluid rheology may significantly impact mixer performance in real-world applications. Non-Newtonian fluids, which are common in biological and industrial applications, may not follow the observed trends. Therefore, future work must investigate the influence of fluid properties in detail and potentially adapt the micromixer design to optimize the performance for specific fluid types.

In conclusion, the presented simulations provide valuable insights into the design optimization of micromixers. They offer a foundation for developing more effective and efficient micromixing strategies, which are critical to applications that range from chemical synthesis to biological assays.

3.3 Mixing performance with different Newtonian fluids

The simulation results of the 3D Tesla micromixer illustrated in Fig. 5 provide significant insights into the effect of fluid viscosity on micromixing efficiency. A coaxial flow was created to initiate the mixing process (Fig. 5a). Three materials with varying viscosities and diffusion coefficients were used to evaluate the performance of the micromixer at different velocities (Figs. 5b–5d).

Fig. 5b depicts the MI as a function of velocity for all three materials. The MI is a quantitative measure of the degree of homogeneity achieved from the mixing process. For all the materials, the MI decreases with the increase in velocity, which indicates that higher flow rates impede the micromixer's ability to achieve homogeneity. This effect is most pronounced for the PGM, which is the fluid with the highest viscosity, where the reduced diffusion coefficient likely hinders the distribution of solute molecules. GM30 and PBS follow a similar trend, although the decline in the mixing efficiency with velocity is less steep for PBS than for GM30, which is consistent with their lower viscosity and higher diffusion rate.

In Fig. 5c, the *Re* is plotted against velocity. For all these materials, the *Re* value initially increases with the velocity, which suggests a transition from laminar flow to a less laminar flow and generally promotes mixing. However, the effectiveness of this transition is highly material-dependent, and PGM and GM30 show a less pronounced increase in *Re*, which is possibly due to the dampening effect of their higher viscosity on turbulence.

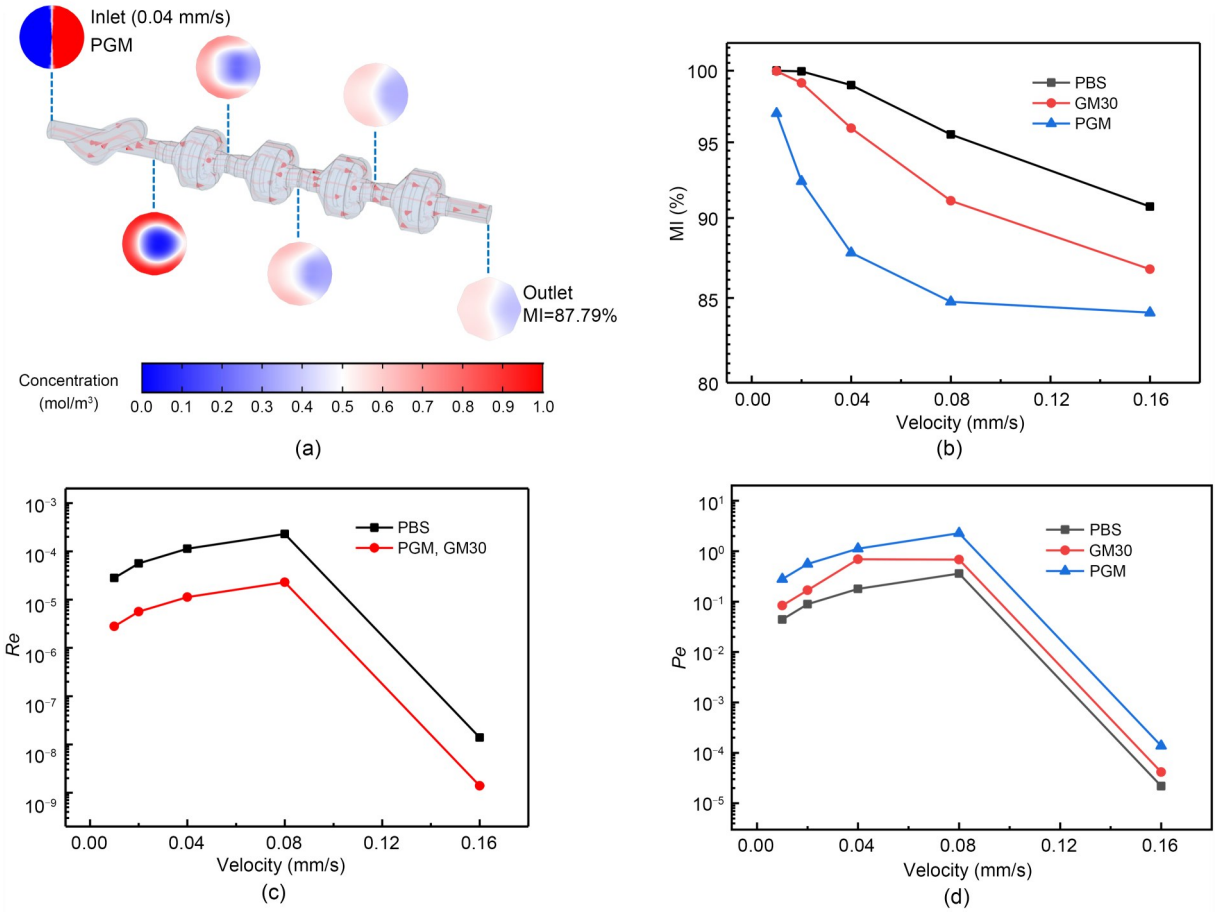

Fig. 5 Simulation results of the 3D Tesla micromixer using different Newtonian fluids: computational simulation results depicting the concentration profile of PGM within a micromixer device (a); mixing index (MI) percentage (b), the Reynolds number (*Re*) (c), and the Péclet number (*Pe*) (d) of the micromixer's performance with varying velocities using three different fluids of phosphate-buffered saline (PBS), GM30 (0.06 g/mL GelMA), and PGM (0.06 g/mL porous GelMA)

The similarity in the trends of all of these materials suggests that while differences in viscosity impact the *Re*, the 3D Tesla micromixer design maintains a degree of robustness across the viscosity range tested.

Fig. 5d represents the *Pe*, which is crucial to assessing the relative contributions of advective transport to diffusive transport. All the materials show an increase in *Pe* with velocity, which implies that advection dominates over diffusion at higher flow rates. This is particularly noticeable for PGM, which exhibits a more significant increase in *Pe* compared with PBS that may be due to its high viscosity and hence low diffusion. This suggests that mixing is less efficient at higher velocities for high-viscosity fluids, as the process is controlled more by the less effective advective transport than by diffusion. With its lower viscosity, PBS displays a lower *Pe*, which indicates a better balance between advection and diffusion and is favorable for mixing.

The 3D Tesla micromixer demonstrated high mixing efficiency with various Newtonian fluids, where each had distinct viscosities and diffusion coefficients. Given this success, our subsequent focus will be on exploring the mixing capabilities of the micromixer with non-Newtonian fluids, which are commonly utilized in bioprinting applications.

3.4 Mixing performance for the non-Newtonian fluid-power-law model

The distinction between the flow behaviors of non-Newtonian and Newtonian fluids has significant implications for the trends observed in Figs. 5 and 6. Non-Newtonian fluids, such as the alginate hydrogel in our case, do not have a constant viscosity; their flow characteristics change with the applied stress or shear rate. A coaxial flow was also produced with non-Newtonian fluids (Fig. 6a). Additionally, the highest velocities indicated in Fig. 6b occur in narrow passages and around the curved obstacles within

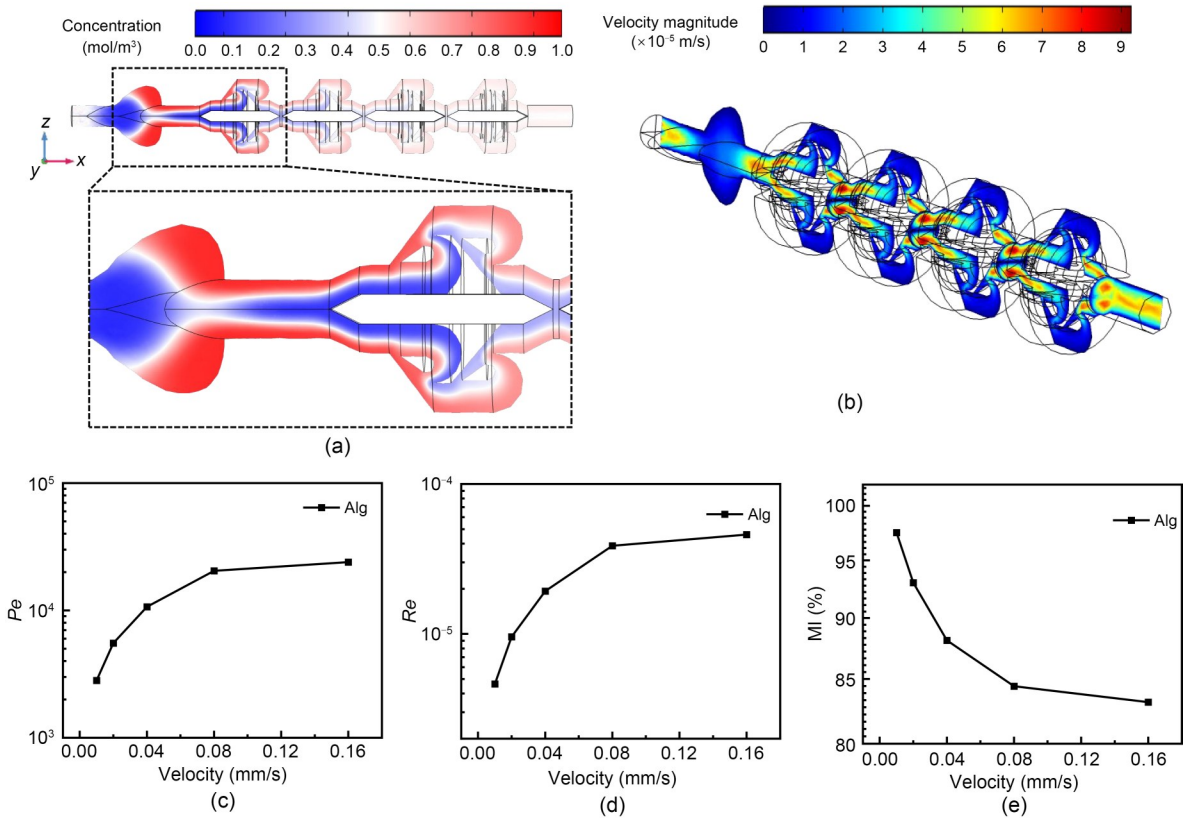

Fig. 6 Computational fluid dynamics (CFD) simulation of a 0.035 g/mL alginate hydrogel (Alg) in a Tesla micromixer treated as a non-Newtonian fluid: concentration profile across the micromixer showing the mixing of two fluids with the progression of flow (a); velocity magnitude slice illustrating complex flow patterns (b); the Péclet number (*Pe*) (c), Reynolds number (*Re*) (d), and mixing efficiency (MI) (e) as a function of the velocity of the flow in the 3D Tesla micromixer. References to color refer to the online version of this figure

the mixer, which may indicate that the design also creates regions of high shear and turbulent flow to enhance the mixing efficiency of non-Newtonian fluids. The blue regions indicate slower flow velocities that may correspond to recirculation zones. In addition, the shear-thinning properties of the fluid dramatically affect the mixing process. Shear-thinning, which is often observed in hydrogels, may lead to enhanced mixing due to a decrease in viscosity with increased shear rate. This would be consistent with the complex flow patterns and color gradients that indicate good mixing in Fig. 6c. However, this also means that the mixing efficiency may be highly dependent on the flow rate and the specific rheological properties of the fluid.

In contrast, the mixing efficiency of Newtonian fluids tends to be more predictable and less sensitive to changes in shear rates. The data previously presented for Newtonian fluids, such as PBS, show how the mixer performs across different velocities, and where the MI decreases as the velocity increases. This trend could be attributed to the fact that at higher velocities, the time for diffusion and homogenization within the mixer is shorter, which leads to less efficient mixing. A more linear relationship between velocity and mixing efficiency for Newtonian fluids simplifies the design and optimization of micromixers.

In conclusion, our 3D Tesla micromixer is adept at handling the intricate dynamics of non-Newtonian fluids, whose mixing is complicated by a viscosity that varies with the flow conditions. This capability is crucial, as non-Newtonian fluids are prevalent in specialized applications such as biomedical engineering and materials science, where consistent and thorough mixing is indispensable. The micromixer's efficiency with these fluids is highlighted by its ability to adapt to their complex rheological properties to ensure thorough mixing.

3.5 Experimental assessment of 3D Tesla micromixer for extrusion 3D printing applications

The 3D Tesla micromixer presents distinct advantages for micromixing applications and 3D printing applications (Figs. 7a, 7b-i, and 7b-ii). The transparency of the material serves a dual purpose: it allows for the real-time visual monitoring of the fluid dynamics within the microchannels, and it facilitates the immediate detection of anomalies such as clogging—a common issue that can significantly disrupt microfluidic processes. This visual accessibility is invaluable for rapid diagnostics and quality control during the mixing process, and it allows for the immediate assessment of the compatibility and homogeneity of different materials as they are combined within the mixer. Furthermore, the design considerations for the Tesla micromixer extend beyond its functional capabilities; its form factor is tailored for seamless integration into existing bioprinting setups. This plug-and-play compatibility is essential to the adoption of new microfluidic devices in complex bioprinting workflows where minimizing setup time and operational complexity is crucial.

In our study, the performance of the micromixer was evaluated using a 0.035 g/mL alginate hydrogel, which is a key component in contemporary bioprinting practices. This choice was instrumental due to its widespread application in the field. To adapt to the challenges associated with low extrusion rates and small outlet diameters in bioprinting, we utilized a technique where the hydrogel is extruded into a $CaCl_2$ bath, which results in droplet formation (Figs. 7c-i and 7c-ii). This method effectively addresses technical limitations while enabling a thorough examination of the mixer's efficiency.

One significant aspect of our analysis was the examination of color uniformity within individual droplets, as assessed in the CIELab color space (Fig. 7c-iii). We found that the Euclidean distance between the colors within the same droplet was consistently less than 4. This result is particularly noteworthy, as it demonstrates the effective mixing of blue and yellow inks. Specifically, for a perfusion of 100% blue and 0% yellow, we observed an error margin of 3.291±0.456; for a 50% blue and 50% yellow mix, the error was 2.040±0.650; for 0% yellow and 100% blue, the error recorded was 3.854±0.890. These findings suggest a high degree of homogeneity in the color mixing within each droplet, which underscores the micromixer's capability to consistently blend the two inks. This ability to maintain such uniformity in coloration irrespective of the perfusion ratios highlights the potential of our micromixer in applications where

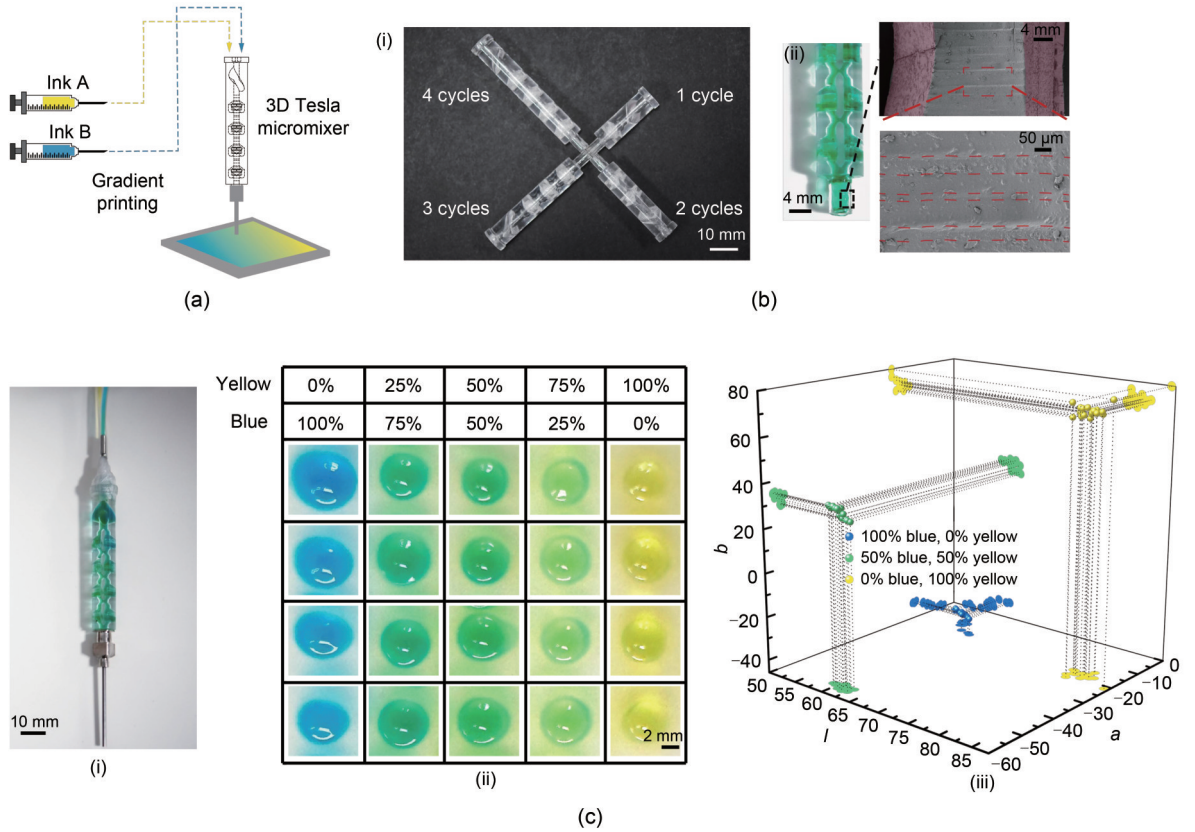

Fig. 7 Multifaceted analysis of gradient droplet generation using a Tesla micromixer: (a) schematic of the experimental setup for bioprinting gradient droplets; (b-i) micromixer variants with increasing cycle iterations to enhance mixing efficiency; (b-ii) scanning electron microscopy image detailing the surface roughness of the micromixer nozzle; (c-i) actual nozzle connected to the micromixer for scale; (c-ii) array of droplets exhibiting color gradients, which are representative of different mixing ratios; (c-iii) color space analysis in CIELab to evaluate the uniformity of droplet coloration within individual droplets and across batches and validate the precision of the mixing process. References to color refer to the online version of this figure

the precise control of material composition is critical, and it marks a significant advancement in bioprinting techniques.

The remarkable mixing performance that we observed experimentally surpassed the outcomes predicted by the simulations. This suggests that the surface roughness of the mixer introduces beneficial flow characteristics that were ignored in the simulation model (Fig. 7b-i). These characteristics likely include the introduction of microscale turbulence and complex flow patterns due to the nuanced geometries inherent in 3D-printed structures. These flow enhancements, which result from the subtle imperfections and surface textures of 3D printing (Fig. 7b-ii), are difficult to predict computationally but have a pronounced impact on performance, as evidenced by our experimental results.

The enhanced performance of the 3D Tesla micromixer, as evidenced by its superior mixing capabilities, marks it as an invaluable tool in bioprinting and demonstrates its remarkable potential in broader applications such as hydrogel mixing. The micromixer's ability to handle the various flow properties of hydrogels underscores its versatility and makes it an ideal component for high-precision mixing tasks. This adaptability extends to the realm of polymer 3D printing, in which the micromixer could revolutionize the process by enabling a more uniform and consistent mixing of polymers, which is a crucial factor in achieving optimal print quality and material properties.

In the context of bioprinting, the 3D Tesla micromixer's capacity for producing homogeneously mixed bioinks is critical. It opens up new avenues for fabricating tissue constructs with precisely controlled

biochemical gradients and cellular distributions. This capability is vital for closely emulating the complex structures and functions of natural tissues. As the field of bioprinting advances, the 3D Tesla micromixer is poised to become a cornerstone in the development of complex, multifunctional tissues. Its contribution is expected to significantly advance the science of tissue engineering and expand its practical applications, thereby paving the way for groundbreaking innovations in medical research and therapeutic interventions.

4 Conclusions

The novel micromixer design introduced in this study demonstrates an enhanced capability for achieving high mixing efficiency with a smaller number of cycles, which is a crucial advancement in bioprinting complex tissue structures. Through rigorous CFD simulations and experimental validation, we established a profound understanding of the dynamics within the micromixer that led to the efficient blending of hydrogels with remarkable reproducibility. This advancement can enhance the precision and consistency of bioprinted structures and pave the way for new possibilities in regenerative medicine and therapeutic applications. Our findings underscore the potential of innovative engineering solutions to overcome the current limitations of bioprinting technologies, and significantly contribute to the advancement of tissue engineering while opening new pathways for future research and clinical applications.

Acknowledgments

This work is supported by the National Key Research and Development Program of China (No. 2018YFA0703000) and the National Natural Science Foundation of China (No. 52275294).

Author contributions

Abdellah AAZMI did most of the experiments and wrote most of the manuscript. Zixian GUO did some part of the writing. Haoran YU set up the printing system for the experiments. Weikang LV and Zengchen JI discussed and edited the manuscript. Huayong YANG provided the resources. Liang MA supervised the manuscript process, and reviewed and edited the manuscript.

Conflict of interest

Abdellah AAZMI, Zixian GUO, Haoran YU, Weikang LV, Zengchen JI, Huayong YANG, and Liang MA declare that they have no conflict of interest.

References

Aazmi A, Zhou HZ, Lv WK, et al., 2022. Vascularizing the brain in vitro. *iScience*, 25(4):104110. https://doi.org/10.1016/j.isci.2022.104110

Aazmi A, Zhang D, Mazzaglia C, et al., 2024. Biofabrication methods for reconstructing extracellular matrix mimetics. *Bioactive Materials*, 31:475-496. https://doi.org/10.1016/j.bioactmat.2023.08.018

Abolpour B, Hekmatkhah R, Shamsoddini R, 2022. Optimum design for the Tesla micromixer. *Microfluidics and Nanofluidics*, 26(6):46. https://doi.org/10.1007/s10404-022-02530-6

Agrawal R, Kumar A, Mohammed MKA, et al., 2023. Biomaterial types, properties, medical applications, and other factors: a recent review. *Journal of Zhejiang University-SCIENCE A (Applied Physics & Engineering)*, 24(11): 1027-1042. https://doi.org/10.1631/jzus.A2200403

Armeniades CD, Johnson WC, Thomas R, 1966. Mixing Device. US Patent 3286992.

Bayareh M, Ashani MN, Usefian A, 2020. Active and passive micromixers: a comprehensive review. *Chemical Engineering and Processing-Process Intensification*, 147: 107771. https://doi.org/10.1016/j.cep.2019.107771

Becker E, 1980. Simple non-Newtonian fluid flows. *Advances in Applied Mechanics*, 20:177-226. https://doi.org/10.1016/S0065-2156(08)70234-5

Bolívar-Monsalve EJ, Ceballos-González CF, Borrayo-Montaño KI, et al., 2021. Continuous chaotic bioprinting of skeletal muscle-like constructs. *Bioprinting*, 21:e00125. https://doi.org/10.1016/j.bprint.2020.e00125

Buglie WLN, Tamrin KF, Sheikh NA, et al., 2022. Enhanced fluid mixing using a reversed multistage Tesla micromixer. *Chemical Engineering & Technology*, 45(7):1255-1263. https://doi.org/10.1002/ceat.202200055

Chávez-Madero C, de León-Derby MD, Samandari M, et al., 2020. Using chaotic advection for facile high-throughput fabrication of ordered multilayer micro- and nanostructures: continuous chaotic printing. *Biofabrication*, 12(3):035023. https://doi.org/10.1088/1758-5090/ab84cc

Chen YB, Niu ZH, Jiang WQ, et al., 2021. 3D-printed models improve surgical planning for correction of severe post-burn ankle contracture with an external fixator. *Journal*

of Zhejiang University-SCIENCE B (Biomedicine & Biotechnology), 22(10):866-875. https://doi.org/10.1631/jzus.B2000576

Florián-Algarín V, Acevedo A, 2010. Rheology and thermotropic gelation of aqueous sodium alginate solutions. *Journal of Pharmaceutical Innovation*, 5(1):37-44. https://doi.org/10.1007/s12247-010-9078-y

Holmberg S, Garza-Flores NA, Almajhadi MA, et al., 2021. Fabrication of multilayered composite nanofibers using continuous chaotic printing and electrospinning: chaotic electrospinning. *ACS Applied Materials & Interfaces*, 13(31):37455-37465. https://doi.org/10.1021/acsami.1c05429

Khandelwal V, Dhiman A, Baranyi L, 2015. Laminar flow of non-Newtonian shear-thinning fluids in a T-channel. *Computers & Fluids*, 108:79-91. https://doi.org/10.1016/j.compfluid.2014.11.030

King RP, 2002. Non-Newtonian slurries. *In*: King RP (Ed.), Introduction to Practical Fluid Flow. Butterworth-Heinemann, Oxford, UK, p.117-157. https://doi.org/10.1016/B978-075064885-1/50005-3

Kokkinis D, Bouville F, Studart AR, 2018. 3D printing of materials with tunable failure via bioinspired mechanical gradients. *Advanced Materials*, 30(19):1705808. https://doi.org/10.1002/adma.201705808

Liu WJ, Zhang YS, Heinrich MA, et al., 2017. Rapid continuous multimaterial extrusion bioprinting. *Advanced Materials*, 29(3):1604630. https://doi.org/adma.201604630

Ma JY, Lin YB, Chen XL, et al., 2014. Flow behavior, thixotropy and dynamical viscoelasticity of sodium alginate aqueous solutions. *Food Hydrocolloids*, 38:119-128. https://doi.org/10.1016/j.foodhyd.2013.11.016

Mehta V, Rath SN, 2021. 3D printed microfluidic devices: a review focused on four fundamental manufacturing approaches and implications on the field of healthcare. *Bio-Design and Manufacturing*, 4(2):311-343. https://doi.org/10.1007/s42242-020-00112-5

Monzón M, 2018. Biomaterials and additive manufacturing: osteochondral scaffold innovation applied to osteoarthritis (BAMOS project). *Journal of Zhejiang University-SCIENCE A (Applied Physics & Engineering)*, 19(4):329-330. https://doi.org/10.1631/jzus.A18NW001

Nguyen NT, Wu ZG, 2005. Micromixers—a review. *Journal of Micromechanics and Microengineering*, 15(2):R1-R16. https://doi.org/10.1088/0960-1317/15/2/R01

Nyande BW, Thomas KM, Lakerveld R, 2021. CFD analysis of a kenics static mixer with a low pressure drop under laminar flow conditions. *Industrial & Engineering Chemistry Research*, 60(14):5264-5277. https://doi.org/10.1021/acs.iecr.1c00135

Poologasundarampillai G, Haweet A, Jayash SN, et al., 2021. Real-time imaging and analysis of cell-hydrogel interplay within an extrusion-bioprinting capillary. *Bioprinting*, 23:e00144. https://doi.org/10.1016/j.bprint.2021.e00144

Ramezani H, Zhou LY, Shao L, et al., 2020. Coaxial 3D bioprinting of organ prototyps from nutrients delivery to vascularization. *Journal of Zhejiang University-SCIENCE A (Applied Physics & Engineering)*, 21(11):859-875. https://doi.org/10.1631/jzus.A2000261

Rastogi P, Kandasubramanian B, 2019. Review of alginate-based hydrogel bioprinting for application in tissue engineering. *Biofabrication*, 11(4):042001. https://doi.org/10.1088/1758-5090/ab331e

Rodríguez-Rivero C, Hilliou L, Martín del Valle EM, et al., 2014. Rheological characterization of commercial highly viscous alginate solutions in shear and extensional flows. *Rheologica Acta*, 53(7):559-570. https://doi.org/10.1007/s00397-014-0780-4

Sánchez-Sánchez R, Rodríguez-Rego JM, Macías-García A, et al., 2023. Relationship between shear-thinning rheological properties of bioinks and bioprinting parameters. *International Journal of Bioprinting*, 9(2):687. https://doi.org/10.18063/ijb.687

Skylar-Scott MA, Mueller J, Visser CW, et al., 2019. Voxelated soft matter via multimaterial multinozzle 3D printing. *Nature*, 575(7782):330-335. https://doi.org/10.1038/s41586-019-1736-8

Tavafoghi M, Darabi MA, Mahmoodi M, et al., 2021. Multimaterial bioprinting and combination of processing techniques towards the fabrication of biomimetic tissues and organs. *Biofabrication*, 13(4):042002. https://doi.org/10.1088/1758-5090/ac0b9a

Valdés JP, Kahouadji L, Matar OK, 2022. Current advances in liquid–liquid mixing in static mixers: a review. *Chemical Engineering Research and Design*, 177:694-731. https://doi.org/10.1016/j.cherd.2021.11.016

Xiong YT, Kang HY, Zhou HZ, et al., 2022. Recent progress on microfluidic devices with incorporated 1D nanostructures for enhanced extracellular vesicle (EV) separation. *Bio-Design and Manufacturing*, 5(3):607-616. https://doi.org/10.1007/s42242-022-00195-2

Zhang B, Xue Q, Hu HY, et al., 2019. Integrated 3D bioprinting-based geometry-control strategy for fabricating corneal substitutes. *Journal of Zhejiang University-SCIENCE B (Biomedicine & Biotechnology)*, 20(12):945-959.

https://doi.org/10.1631/jzus.B1900190

Zhang HL, Yao Y, Hui Y, et al., 2022. A 3D-printed microfluidic gradient concentration chip for rapid antibiotic-susceptibility testing. *Bio-Design and Manufacturing*, 5(1): 210-219.
https://doi.org/10.1007/s42242-021-00173-0

Zhou HZ, Liu P, Gao ZQ, et al., 2022. Simultaneous multimaterial multimethod bioprinting. *Bio-Design and Manufacturing*, 5(3):433-436.
https://doi.org/10.1007/s42242-022-00203-5